Journal of Materials Chemistry C

ROYAL SOCIETY OF CHEMISTRY

PAPER

View Article Online
View Journal | View Issue



Cite this: J. Mater. Chem. C, 2023, 11, 13981

# Gate-tunable rectification and photoresponse in a $MoTe_2/SnS_2$ van der Waals heterostructure based P–N diode†

Ehsan Elahi,*[a] Muhammad Asghar Khan,[a] Jaeho Jeon,[a] Sahng-Kyoon Jerng,[a] Abdullah A. Al-Kahtani[b] and Hwayong Noh*[a]

Received 8th June 2023,
Accepted 22nd September 2023

DOI: 10.1039/d3tc01990j

rsc.li/materials-c



The p–n junction, one of the prominent electrical components capable of being utilized in electronics and optoelectronics, has attracted renewed interest due to recent research in two-dimensional (2D) materials. In this work, we constructed a heterostructure p–n diode based on $MoTe_2$ and $SnS_2$. Sweeping the back-gate voltage ($V_{bg}$) effectively results in a high rectification ratio of $2.79 \times 10^5$ at $V_{bg}$ = +10 V and the lowest ideality factor ($\eta$) of about 1.25 was achievedwhen $V_{bg}$ = −30 V. The interlayer electron–hole recombination is responsible for the variation in rectification behavior. This photodiode exhibits effective photodetection capabilities and promising merit statistics. The maximum change in photocurrent ($I_{ph}$) is measured to be about 90 nA at $V_{ds}$ = 0.9 V, and the device exhibited a high responsivity ($R$) of $5.8 \times 10^4$ mA $W^{-1}$, while the maximum external quantum efficiency (EQE) and detectivity are calculated to be about $3.27 \times 10^4$ (%) and $2.47 \times 10^{10}$ Jones for the device, respectively, when illuminated with 220 nm wavelength incident light at a power intensity of 11 mW $cm^{-2}$. The average rise/fall times for the 220 nm wavelength at $V_{ds}$ = 0.9 V are observed to be 0.29 s/0.38 s, respectively. We examined the photoresponse of the device as a function of time at different wavelengths ($\lambda$ = 970–220 nm) of the incident light and at different power intensities ($P$ = 11–44 mW $cm^{-2}$) of the incident light. The maximum values of $V_{oc}$ = 0.32 V and $I_{sc}$ = −0.40 nA were achieved at $P$ = 44 mW $cm^{-2}$. The p-$MoTe_2$/n-$SnS_2$-based device has excellent rectifying and optoelectronic properties.

## Introduction

Two-dimensional (2D) layered materials are considered to have outstanding potential in electronics and optoelectronics due to their desirable physical characteristics.[1,2] Because of their customized energy band alignments and ultrathin structural characteristics, van der Waals (vdW) heterojunctions established on thin 2D materials have ushered in a new era for next-generation optoelectronics.[3] Graphene has received a great deal of attention in the fields of spintronics,[4–6] electronics,[7] and optoelectronics.[7,8] In another class, depending on the layer thickness, 2D transition metal dichalcogenide (TMDC) materials have band gaps between 1 eV and 2.5 eV. A broad range of applications, including photodetectors,[9,10] field-effect transistors,[11,12] flexible devices,[13] logic circuits,[14] and optical communication,[15,16] are possible due to the band gap variation between the multilayer indirect gap and the monolayer direct gap.[17,18] Ever more research has focused on p–n junctions made of various 2D layered materials, creating a new material platform for investigating novel physical features and new device applications.[19–21] One may tune the energy band alignment by joining individual layers of different 2D layered materials for the vdW heterostructure with a sharp junction at the atomic scale. This provides a wealth of options for investigating the fundamentals of new electrical and optical features. Thus, TMDCs/TMDCs or TMDCs/graphene heterostructures have been the focus of current studies in the field of 2D TMDCs.[22,23] In addition, due to their ultrathin nature and steep interfacial charge-carrier gradient, 2D vdW heterostructures have significant tunability in band alignment and carrier density, providing an alternative avenue for versatile electrical and optoelectronic applications. For example, in atomically thin GaTe/$MoS_2$ and $WSe_2/MoS_2$ p–n heterojunctions, the external quantum efficiency (EQE) of 40–60% is attained.[23,24] In addition, photodetectors based on $MoTe_2/MoS_2$ vdW heterojunctions are also demonstrated,[25,26] and gate-tunable photovoltaic behavior is also seen in $WSe_2/MoS_2$ heterojunctions.[27]

[a] Department of Physics & Astronomy, Sejong University, 209 Neungdong-ro, Gwangjin-Gu, Seoul, 05006, South Korea. E-mail: Ehsanelahi@sju.ac.kr, hnoh@sejong.ac.kr
[b] Chemistry Department, Collage of Science, King Saud University, P. O. Box 2455, Riyadh 11451, Saudi Arabia

† Electronic supplementary information (ESI) available. See DOI: https://doi.org/10.1039/d3tc01990j

Gate tunable rectification and photoresponse of the heterostructure GeSe/$WS_2$ based p–n diode were also observed.[28] Yet, due to the limited photocurrent flow without an external bias control, the responsivity of such devices remains low. As a result, greater efforts are required to increase the effectiveness of photodetectors based on TMDCs for future nanoscale optoelectronic devices. Molybdenum ditelluride ($MoTe_2$) has played a significant role in electronic devices. $MoTe_2$ exhibits a direct band gap that ranges from 0.9 to 1.1 eV, depending on the material's thickness and lattice structure.[29] $MoTe_2$ has potential use in a variety of devices, including digital logic circuits,[30] solar cells,[31] and chemical sensors[32] owing to its effective mobility and lack of dangling bonds. $SnS_2$ offers intriguing opportunities for creating heterostructures with other 2D materials with various crystallographic structures. A band gap of 2.28 eV is thus found that corresponds to the band gap of $SnS_2$.[33] $SnS_2$ has been identified as an n-type semiconductor because of its technological significance for next-generation electronic/photonic applications. Thus, layered two-dimensional (2D) $SnS_2$ has garnered significant interest.[34,35]

Here, we present a heterostructure p–n diode consisting of $MoTe_2$ and $SnS_2$. Sweeping the back-gate voltage effectively results in a high rectification ratio of $2.79 \times 10^5$. The variance in rectification behavior is caused by interlayer electron–hole recombination. Effective photodetection and inspiring merit statistics characterize this photodiode. The maximum change in photocurrent ($I_{ph}$) is measured to be about 90 nA. The device exhibited a high responsivity ($R$) of $5.8 \times 10^4$ mA $W^{-1}$, while the maximum external quantum efficiency (EQE) and detectivity ($D^*$) are calculated to be about $3.27 \times 10^4$ (%) and $2.47 \times 10^{10}$ Jones for the device when illuminated with incident light at a wavelength ($\lambda$) of 220 nm and a $V_{ds}$ of 0.9 V, respectively. Furthermore, the photoresponse of the device was investigated under the illumination of light of various wavelengths and at different power intensities of incident light. The p-$MoTe_2$/n-$SnS_2$-based device exhibits remarkable optoelectronic and rectifying characteristics.

## Device fabrication and characterization

Thin layers of $MoTe_2$ and $SnS_2$ were formed using the mechanical exfoliation method. Using an adhesive tape, flakes of both materials were mechanically exfoliated. These were then captured by a polydimethylsiloxane (PDMS) stamp on a glass slide as part of the transfer procedure. By positioning the PDMS stamp on a $Si/SiO_2$ substrate and peeling it off, few layers of $SnS_2$ and then $MoTe_2$ are transferred to the target substrate using the dry transfer method. A micro-aligner stage was used to carefully manage the transfer of each flake, which was monitored by a CCD camera. Then the substrate containing these layers (heterojunction) was dipped into acetone/methanol for 2 hours for the removal of residues. After this, the substrate was dried using nitrogen ($N_2$) gas. Polymethylmethacrylate (PMMA) was coated on the substrate that contains the heterostructure of $MoTe_2$–$SnS_2$, and contact electrode patterns were formed by e-beam lithography on the layer. Then the contact electrodes composed of Cr/Au (5 nm/60 nm) were deposited using a thermal evaporator. Then, the substrate was placed in acetone/methanol for the removal of unwanted metals, after this the substrate was dried using nitrogen gas. Finally, we connected the gate at the back ($V_{bg}$: back gate) of the $Si/SiO_2$ substrate with indium wire. The schematic of the device that contains the heterostructure of $MoTe_2$–$SnS_2$ is illustrated in Fig. 1(a). The scanning electron microscopy (SEM) image of the $MoTe_2$–$SnS_2$-based device is presented in Fig. 1(b). An atomic force microscope (AFM: Nano Focus) is employed to verify the thickness of the heterostructure. Fig. 1(c) depicts the AFM image of the device and thickness of the heterostructure of $MoTe_2$–$SnS_2$. The Renishaw spectrometer with a 514 nm excitation wavelength is utilized to check the Raman spectra. The Raman peak shows the basic characteristics of the $MoTe_2$–$SnS_2$ heterojunction as shown in Fig. 1(d). Two peaks can be seen in the Raman spectra of $MoTe_2$ at 172.4 $cm^{-1}$ and 232.9 $cm^{-1}$, respectively. These peaks correspond to the out-of-plane vibrational mode $A_{1g}$ and the in-plane vibrational mode $E^1{}_{2g}$, and the $A_{1g}$ mode at 315.7 $cm^{-1}$ corresponds to $SnS_2$. The individual Raman spectra of both $MoTe_2$ and $SnS_2$ are presented in Fig. S1(a and b) (ESI†). For $SnS_2$, in the heterojunction region, the peak got contribution of both materials, representing the presence of two different materials. Specifically, a reduction in the peak intensity for $SnS_2$ due to screening from $MoTe_2$ is clearly observed. In addition, we have observed a minor blue shift for the peak corresponding to $A_{1g}$, this may be due to the transfer of holes from $MoTe_2$ to $SnS_2$ material, and a minor blue shift is also seen in the peaks of $MoTe_2$ after stacking with $SnS_2$.

We created intensity maps to visualize their spatial distribution across the heterostructure. These maps represent the variation in Raman intensity at specific Raman shift values and provide insights into the distribution and interaction of the materials within the heterostructure. We have observed the Raman intensity of $MoTe_2$/$SnS_2$, which shows that the $MoTe_2$ and $SnS_2$ grains are laterally and flawlessly spliced in the heterostructure without the construction of alloy phases at their junction. The area selected for Raman mapping investigated is highlighted in Fig. 2(a). Graphical depiction of the Raman intensity mapping obtained at 172.43 ($A_{1g}$), and 232.93 $cm^{-1}$ ($E^1{}_{2g}$) for $MoTe_2$, and 315.78 $cm^{-1}$ ($A_{1g}$) for $SnS_2$ is shown in Fig. 2(b–d). The Raman mapping data show the perfect formation of the vdW heterostructure based on $MoTe_2$–$SnS_2$.

The materials $MoTe_2$ and $SnS_2$ were characterized by X-ray photoelectron spectroscopy (XPS). We have utilized an XPS (PHI 5000 Versa Probe III, ULVAC PHL, Japan), with a monochromatic Al Kα (1486.6 eV) X-ray source with a beam spot size of ~20 μm. Fig. 3(a and b) shows the XPS spectra of Mo and Te, and the fitted peaks for the $MoTe_2$ flake are consistent with the previously reported results.[36] The corresponding valence band maximum (VBM) spectra of $MoTe_2$ are presented in Fig. 3(c) and are valued at ~0.10 eV. Fig. 3(d and e) shows the XPS

 

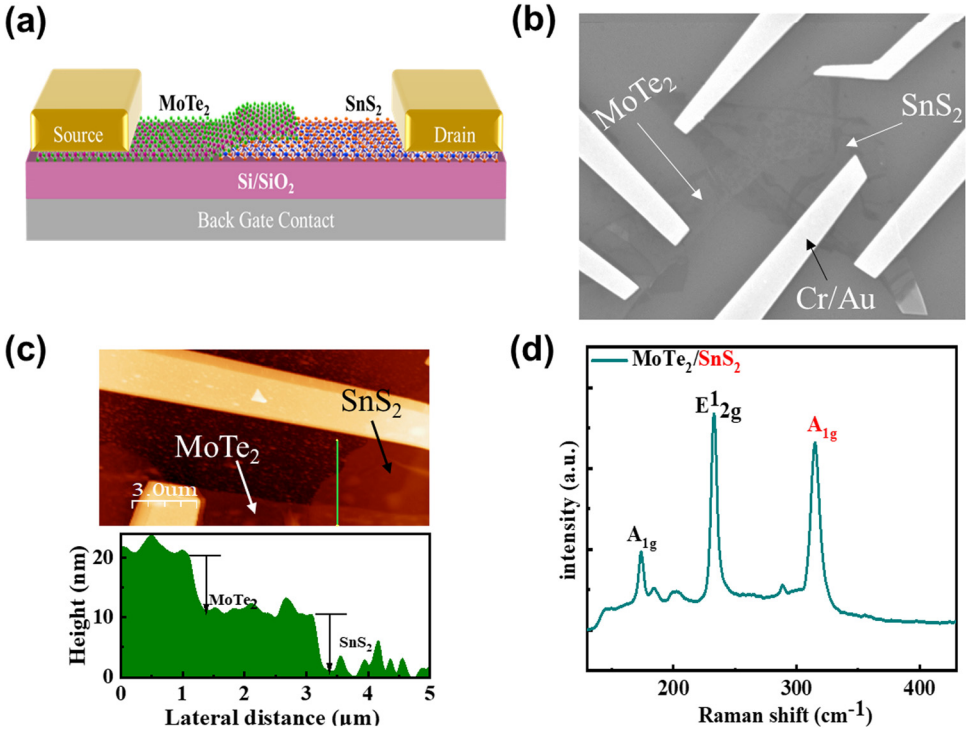


Fig. 1 (a) Schematic illustration of the p–n device. (b) SEM image of the p–n heterostructure $MoTe_2$–$SnS_2$-based device; the scale bar is 5 μm. (c) AFM profile of the heterostructure. (d) Raman spectra of the $MoTe_2$–$SnS_2$ heterostructure.

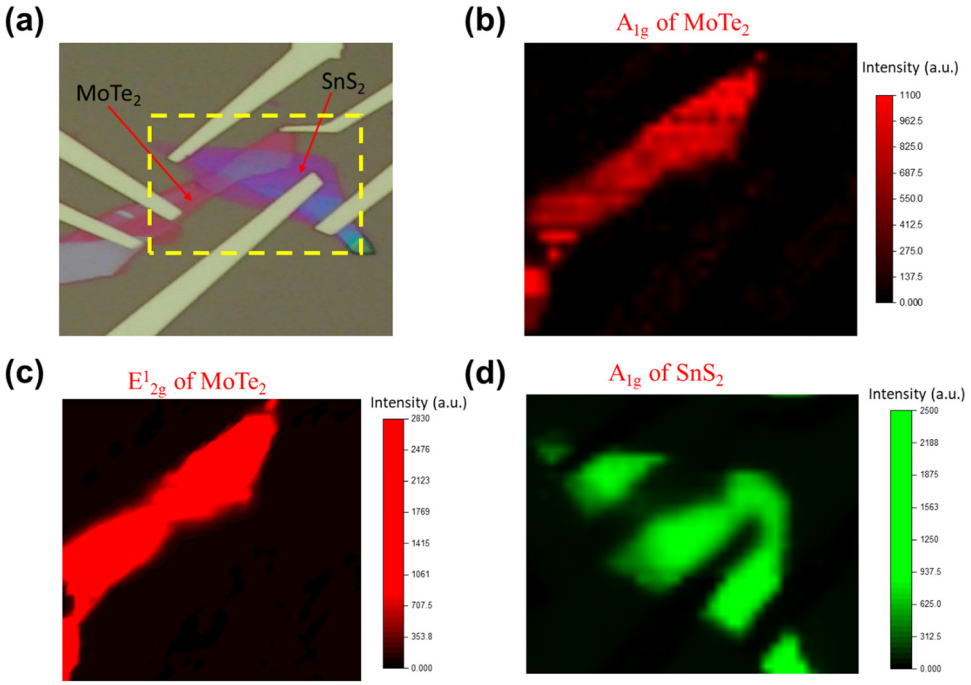


Fig. 2 (a) Optical image of the device that shows the area selected for Raman mapping. (b) Raman intensity maps of $A_{1g}$ of $MoTe_2$. (c) Raman intensity maps of $E^1_{2g}$ of $MoTe_2$. (d) Raman intensity maps of $A_{1g}$ of $SnS_2$. Graphical representation of Raman intensity mapping at 172.43 and 232.93 $cm^{-1}$ for $MoTe_2$, and 315.78 $cm^{-1}$ for $SnS_2$.

spectra of $Sn3d_{5/2}$, $Sn3d_{3/2}$, $S2p_{3/2}$ and $S2p_{1/2}$. The VBM spectra of $SnS_2$ are depicted in Fig. 3(f), which correspond to the value of ~1.53 eV. The fitted Sn and $S_2$ binding energies of $SnS_2$ are in good agreement with the previous report.[37] The XPS peaks are well defined and show that the flakes of $MoTe_2$ and $SnS_2$ are of high quality with no detectable oxidation state present on the

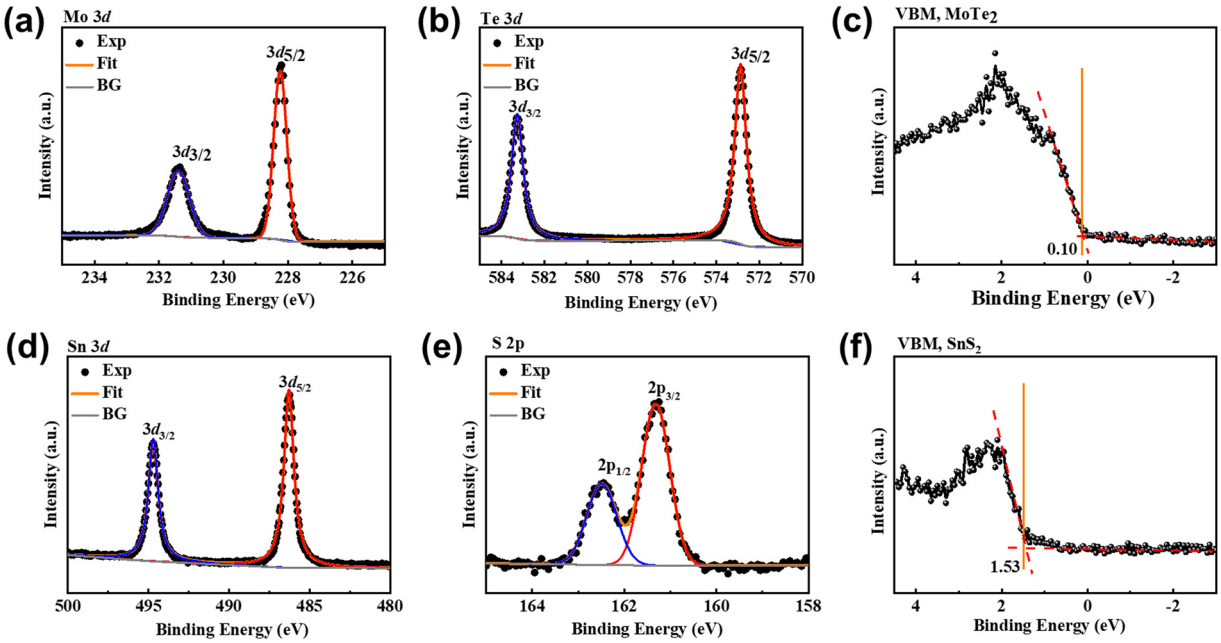


Fig. 3 XPS spectra: (a) Mo 3d peaks. (b) Te 3d peaks. (c) VBM of $MoTe_2$. (d) Sn 3d peaks. (e) S 2p peaks. (f) VBM of $SnS_2$.

surface of flakes. The separation between $Mo3d_{3/2}$ and $VBM_{MoTe2}$ and $Sn3d_{5/2}$ and $VBM_{SnS2}$ is illustrated in Fig. S2(a) (ESI†). Based on the XPS data, we have approximately calculated the band alignment of $MoTe_2$–$SnS_2$-based sample. The valence band offset is observed to be ≈1.43 eV, and the detailed calculation is shown in the ESI.† Based on valence band offset (VBO) approximate data obtained through XPS, we have calculated the conduction band offset (CBO) of 0.25 eV for $MoT_2$–$SnS_2$ and illustrated the band alignment. The detailed calculation is shown in Fig. S2(a and b) (ESI†).

## Results and discussion

### Electrical and photoresponse investigation

The *IV* curves were obtained at various back gate voltages ($V_{bg}$) using a Keithley 2400 (source meter) and a picometer (Keithley 6485) to assess the drain current. The photoresponsivity and EQE were evaluated using a light source of various wavelengths and irradiation power of different intensities. All measurements were taken at room temperature, to allow light illumination of the whole sample, and the device was placed inside a closed glass box under a high vacuum.

### Electrical transport and rectification effects in $MoTe_2$/$SnS_2$ p–n diodes

The electrical characteristics of both materials were examined individually also, and the *I–V* curves of separate $MoTe_2$ and $SnS_2$ at various back gate voltages are exhibited in Fig. S3(a and b) (ESI†). Each $MoTe_2$ and $SnS_2$ transfer curve exhibits obvious p- and n-type characteristics, respectively, as presented in Fig. S3(c and d) (ESI†). The source electrode was linked to $MoTe_2$ (p-type) in our measurement approach, whereas drain contact was linked with $SnS_2$ as indicated in Fig. 1(b). The *I–V* characteristics curves in linear scale for the $MoTe_2$–$SnS_2$ heterostructure at various back gate voltages are illustrated in Fig. 4(a), where the source–drain voltage range is −2 V to +2 V. The IV relation employed for typical p–n diodes made of semiconductors may be utilized to investigate the output properties of vdW's heterojunction-based p–n devices.[38] The following equation provides the value for the current "*I*" *via* the diode:

$$I_D = I_S\left[\exp\left(\frac{qV}{nk_BT}\right) - 1\right] \quad (1)$$

where $I_s$ refers to the saturation current, $k$ is the Boltzmann constant, $\eta$ refers to the ideality factor and $q$ is the electronic charge. The *I–V* curves of the p–n diodes are presented in logarithmic scale as shown in Fig. 4(b). We define the rectification ratio ($R.R = I_f/I_r$) as the fraction of the forward current ($I_f$) and reverse-bias current ($I_r$) in order to test the rectification effect. We have attained a high rectification ratio of $2.79 \times 10^5$ at back gate voltage $V_{bg}$= +10 V during the back-gate sweep effectively. Since $I_r$ reduces more successfully in the negative $V_{bg}$ than in the previously reported BP/$MoS_2$ configuration, the *R.R* value is increased further three times.[39,40] The high rectification rate is ascribed to two causes. The larger barrier height for $V_{bg} < 0$ V is the first explanation for the reduced reverse-bias leakage current. Expectedly, the barrier height between $MoTe_2$ and $SnS_2$ decreases for the positive $V_{bg}$, which in turn brings down the depletion width. Similar to this, a negative $V_{bg}$ raises the barrier height and widens the depletion breadth. The tuning of the Schottky barrier (SB) height through gate-voltage at the metal/TMDC contact is the additional factor that causes the enhancement of the rectification ratio. The variation in the rectification ratio of the device at various gate voltages is

 

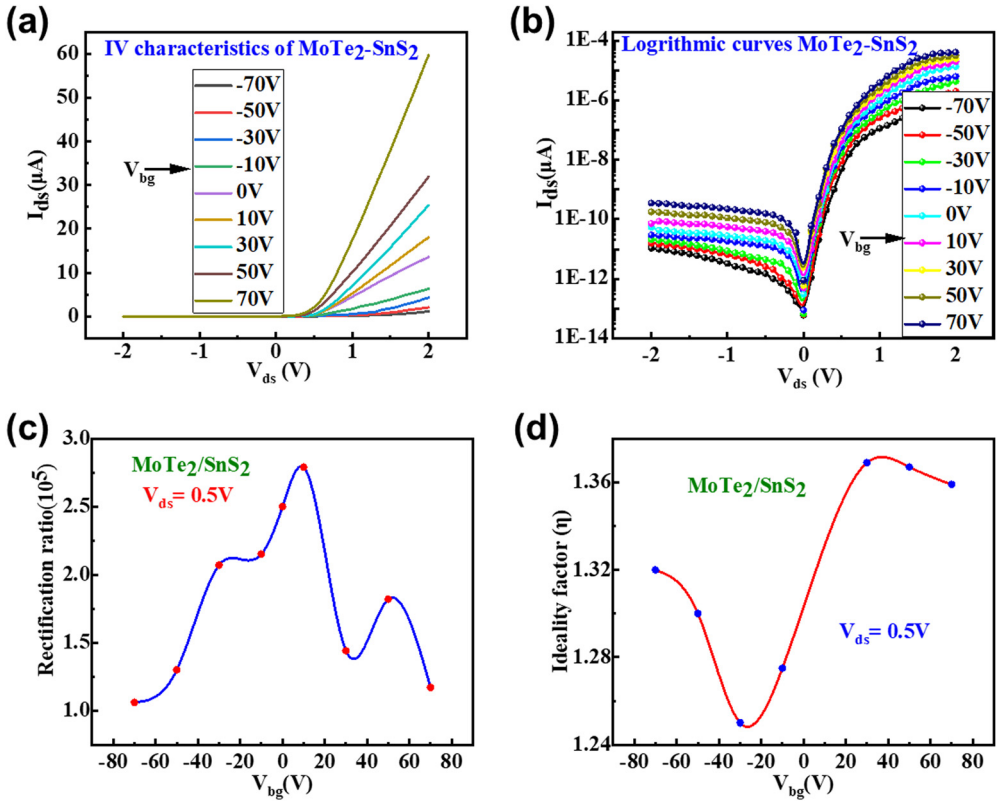


Fig. 4 (a) $I_{ds}$–$V_{ds}$ characteristic curves of the $MoTe_2$–$SnS_2$ heterostructure at various back gate voltages ($V_{bg}$); the linear scale. (b) Logarithmic scale. The maximum rectification ratio is 2.79 × $10^5$ mA $W^{-1}$. (c) The change in the rectification ratio of the device at various back gate voltages. (d) The variation in the ideality factor at different gate voltages.

illustrated in Fig. 4(c). $V_{bg}$ has a significant impact on the $MoTe_2/SnS_2$ heterojunction p–n diode's output characteristics. The ideality factor at different back gate voltages is calculated; the variation in the ideality factor at various gate voltages is represented in Fig. 4(d). The detailed calculation for the ideality factor is expressed in the ESI† (Fig. S4). The lowest value of ideality is 1.25, which is achieved at $V_{bg}$ = −30 V.

Fig. 5(a) demonstrates the energy-band diagram in p-$MoTe_2$ and n-$SnS_2$ with work functions, conduction band (CB) minima, and valence band (VB) maxima. In the case of $SnS_2$, the Fermi level is close to the CB, which displays n-type behavior, while the Fermi level of $MoTe_2$ is close to the VB, which displays p-type behavior. The band diagram of the $MoTe_2/SnS_2$ vdW heterostructure at zero $V_{bg}$ is shown in Fig. 5(b) along with the associated Fermi level. The second part depicts a zoomed-in picture of the band configuration following the contact with zero $V_{bg}$. The Fermi level may be manipulated using the gate voltage, which modulates the charge carrier densities (holes and electrons) in p-$MoTe_2$ and n-$SnS_2$, correspondingly, and hence the rectification ratio as well. The Fermi

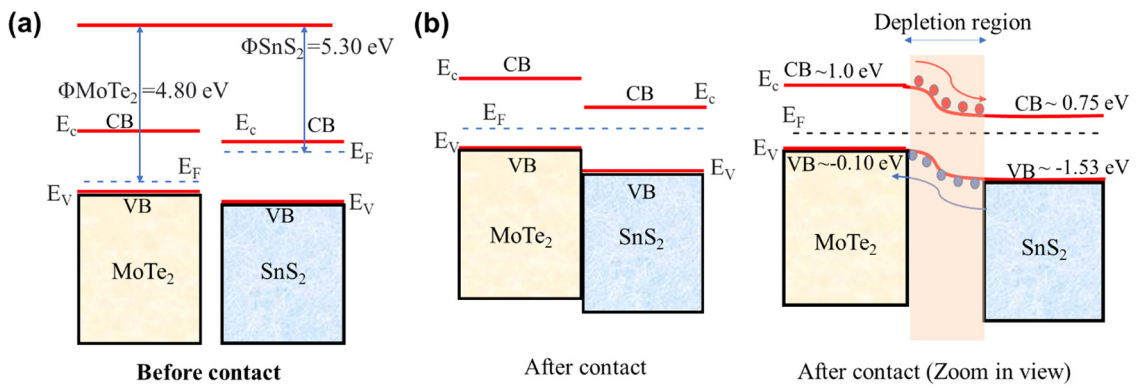


Fig. 5 Schematic illustration of the band diagram for the p-$MoTe_2$/n-$SnS_2$ structure-based diode at $V_{bg}$ = 0 V. (a) Schematic signifies the band diagram of a p-$MoTe_2$/n-$SnS_2$ diode before connection, and (b) symbolizes the diode after connection.

level shifts away from the "CB" at $V_{bg} < 0$ V, increasing the potential barrier at the junction of the $MoTe_2/SnS_2$ vdW heterostructure diode, which generates a strong rectifying current. When $V_{bg} > 0$ V, the Fermi level moves toward the CB, lowering the barrier height. The manipulation of charge carriers (holes and electrons) and band positions of the $MoTe_2/SnS_2$-based diode by gate voltage offers an alternative way to fabricate very competent vdW heterojunctions.

### Optoelectronic properties of $MoTe_2/SnS_2$ p–n diodes

The optoelectronic properties of devices made of 2D materials have been the focus of ongoing research. Because the charge transfer differs from that of common p–n diodes, we studied the photoresponse to further investigate the potential exciting optoelectrical performance. The p-$MoTe_2$/n-$SnS_2$ heterojunction has high photovoltaic capabilities in addition to good electric qualities. The schematic of the photocurrent measurement approach is illustrated in Fig. 6(a), where the device is placed in a glass vacuum chamber. DUV light was beamed on the diode, causing a significant number of electron–hole pairs to form in both the $SnS_2$ and $MoTe_2$ layers. These photoinduced charge carriers penetrate the barrier, producing a strong photoresponse. The individual photocurrents of the 2D layers $MoTe_2$ and $SnS_2$ at different gate voltages are presented in Fig. S5 and S6 (ESI†), respectively. The $MoTe_2/SnS_2$ p–n diode is lit by light with the wavelength ($\lambda$) of 220 nm and an irradiation power ($P$) of 11 mW cm$^{-2}$. The photocurrent of the device at various source–drain voltages ($V_{ds}$) based on the $MoTe_2$–$SnS_2$ heterostructure is shown in Fig. 6(b). This illustrates how the photocurrent changes as a light is turned on and off repeatedly. A probable photo-switching mechanism is suggested by the photocurrent's on-and-off switching behavior. The maximum change in photocurrent ($I_{ph}$) is found to be about 90 nA at $V_{ds}$ = 0.9V. Due to a rise in the built-in potential and charge carrier, we saw that the value of photocurrent rose at higher voltages. The large photovoltaic behavior is caused mostly by type-II band arrangement and a greater built-in potential at the junction, which efficiently distinguishes the photo-excited electron–hole pairs. The device exhibited a high responsivity ($R$) of 5.8 × 10$^4$ mA W$^{-1}$ at $V_{ds}$ = 0.9 V. The following formula is used to derive the photoresponsivity ($R$).

$$R = \frac{I_{ph}}{PA} \quad (2)$$

where $P$ is the incident light power, $A$ is the effective area (14 μm$^2$) and $I_{ph}$ is the photocurrent. The detectivity $D^* = RA^{1/2}/(2e.I_{dark})^{1/2}$ is also calculated, where $R$ denotes responsivity, "$A$" is the effective area, $e$ is the charge of the electron, and $I_{dark}$ is the dark current,[41,42] and the detectivity ($D^*$) is about 2.47 × 10$^{10}$ Jones. The electrons and holes collected in the n-$SnS_2$ and

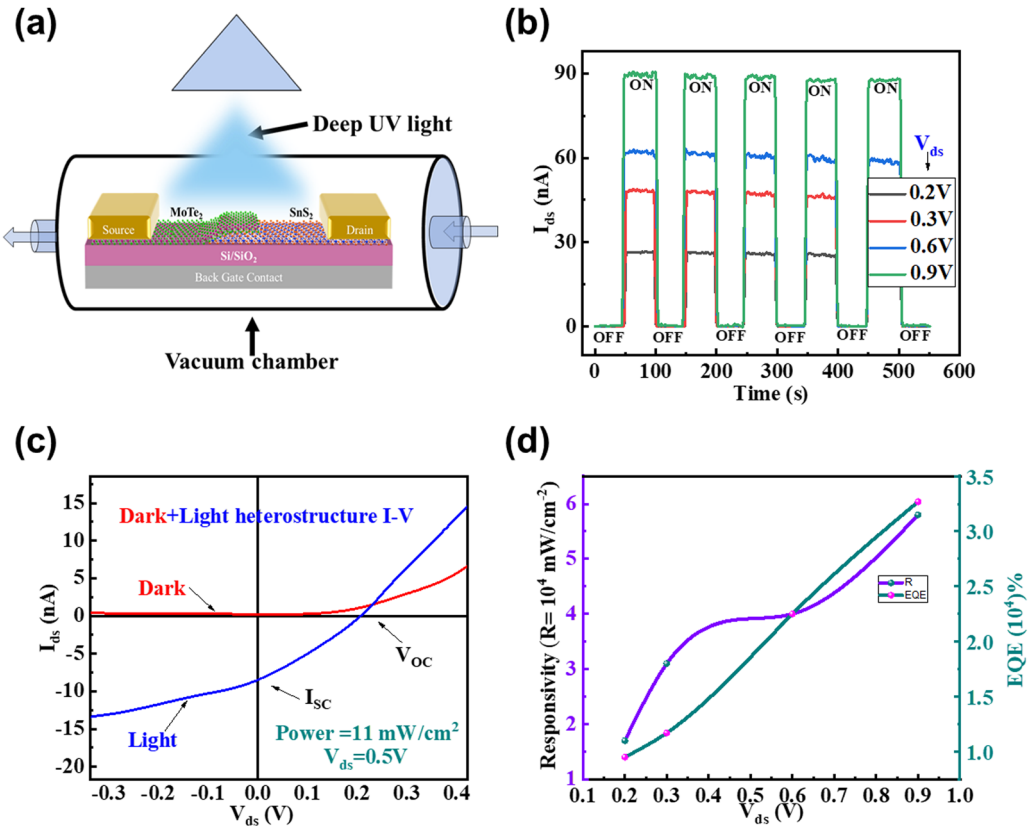


Fig. 6 (a) Schematic of the p–n device for photodetection. (b) Photocurrent at $V_g$ = 0, for $V_{ds}$= 0.2–0.9 V with incident light ($\lambda$ = 220 nm) and power intensity 11 mA cm$^{-2}$. (c) $I$–$V$ curves in the dark and under light, representing $I_{SC}$ = −8.5 nA and $V_{oc}$ = 0.20 V at $V_g$ = 0. (d) The change in responsivity at different values of $V_{ds}$. (e) The enhancement in the EQE at different values of $V_{ds}$.

 

p-$MoTe_2$ layers, respectively, result in the development of an open-circuit voltage ($V_{OC}$). These retrieved electrons and holes in $SnS_2$ and $MoTe_2$ quickly recombine through an external circuit, producing a short-circuit current ($I_{SC}$). At room temperature, our device represented an open circuit voltage ($V_{oc}$) of 0.20 V and a short circuit current ($I_{sc}$) of −8.5 nA and when $V_g$ = 0 as presented in Fig. 6(c). This is due to the high photoabsorption and effective photoinduced electron–hole pair production. The amount of photo-generated carriers per incident photon per second is defined as the EQE, and the following equation was used to obtain the EQE,[43,44]

$$\mathrm{EQE} = R\frac{hc}{e\lambda}\% \quad (3)$$

where '$h$' refers to Plank's constant, $c$ denotes the speed of light, e is the electron charge ($e$), and $\lambda$ is the wavelength of light. The EQE value is determined from light absorption and the buildup of photo-generated carriers. In comparison to all previously reported p–n heterojunctions, we achieved the greatest EQE (%) of $3.27 \times 10^{4\%}$ at $V_{ds}$ = 0.9 V, along with improved responsivity and other electronic/optoelectronic characteristics.[45–47] The change in "$R$" and "EQE" at different $V_{ds}$ is depicted in Fig. 6(d). Moreover, because of the significant built-in potential, a quick photo-carrier separation and the associated short transit time may lead to a significant gain and a significant EQE.[48,49] Fig. 6(b and c) indicate that the rise in the forward- and reverse-bias currents is related to the creation of electron–hole pairs brought on by illumination. When illuminated, the charges are separated at the junction,[50,51] causing the electrons to collect on the top face of the $SnS_2$ and the holes to belong to the bottom face of $MoTe_2$. Due to the formation of dipoles in the junction region, increased electron–hole pair production is subsequently induced.[52] Our $MoTe_2/SnS_2$ heterojunctions were shown to have a significant promise for both electrical and optoelectronic devices due to their effective photoresponsivity and high EQE. Another cause for the high EQE is the built-in voltage at the interface.[24,53] Due to the slight difference among "CB" maximums of $MoTe_2$ and $SnS_2$, electrons and holes recombine in greater quantities at the junction between $MoTe_2$ and $SnS_2$, increasing the built-in potential. Furthermore, it is envisaged that the screening against coulomb impurities would be improved in the devices based on 2D materials, resulting in a larger EQE.[24] The average rise/fall time is 0.29 s/0.38 seen for the wavelength of 220 nm at $V_{ds}$ = 0.9 V, respectively. The fitting/calculation details related to rise/fall time is shown in tabular and graphical form in Fig. S7(a and b) (ESI†).

We have examined the photoresponse of the device as a function of time at different wavelengths ($\lambda$ = 970, 650, 365 and 220 nm) of the incident light at $V_{ds}$ = 0.5 V as shown in Fig. 7(a). The photocurrent of the device is enhanced as the wavelength of incident light is decreased. The observed photocurrent rises as the wavelength decreases, reaching its maximum value at $\lambda$ = 220 nm because of the higher production of electron–hole pairs at low wavelengths. Because there are more excited charge carriers, smaller wavelengths produce greater photocurrent and responsivity values. This behavior is related to strong absorption and high photon energies at low wavelengths, which is compatible with the findings of earlier research.[54] We have

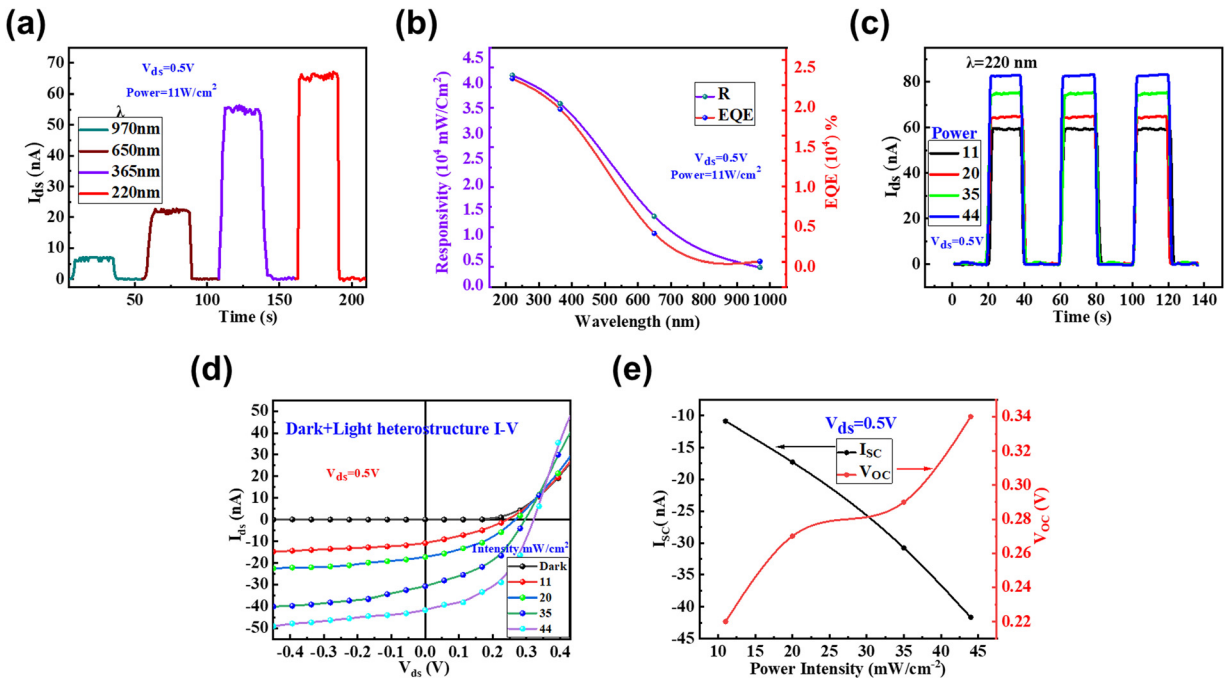


Fig. 7 (a) Photocurrent of the device based on the $MoTe_2/SnS_2$ heterostructure as a function of time at different wavelengths of incident light. (b) Change in $R$ and EQE as a function of wavelength, which shows a decreasing trend. (c) Photoresponse of the device at different power intensities of incident light at the wavelength of 220 nm. (d) $I$–$V$ characteristics curve of the device under the dark and with the radiant light of different power intensities. (e) Variation in $V_{OC}$ and $I_{SC}$ under different power intensities of radiant light ($P$ = 11, 20, 35, 44 mW cm$^{-2}$).

Table 1 The summary of photodetectors based on various 2D materials

| Materials | Wavelength ($\lambda$) | Responsivity | Detectivity ($D^*$) Jones | EQE (%) | Ref. |
|---|---|---|---|---|---|
| $GaSe/PtSe_2$ | 520 nm | 1.78 A $W^{-1}$ | $3.5 \times 10^{12}$ | 405 | 55 |
| $WSe_2/ReS_2$ | 600 nm | 3 A $W^{-1}$ | $8.39 \times 10^{10}$ | 600 | 56 |
| $BP/MoS_2$ | Near IR (532 nm) | 22.3 A $W^{-1}$ | $3.1 \times 10^{11}$ | $\sim 10^3$ | 57 |
| $PtSe_2/GaAs$ | 200–1200 nm | 0.262 A $W^{-1}$ | $2.52 \times 10^{12}$ | — | 58 |
| $GeAs/ReS_2$ | 532 nm | $6.86 \times 10^3$ mA $W^{-1}$ | $1.2 \times 10^9$ | 1639% | 59 |
| | 1550 nm | $1.02 \times 10^2$ mA $W^{-1}$ | $2.16 \times 10^8$ | | |
| $GaSe/MoS_2$ | 520 nm | 0.67 A $W^{-1}$ | $2.3 \times 10^{11}$ | $\sim$160% | 60 |
| $SnS_2$/MXene $Nb_2C$ | 365 nm | 102.44 μA $W^{-1}$ | $7.48 \times 10^{12}$ | — | 61 |
| $GaSe/SnS_2$ | 633 nm | $\sim$35 A $W^{-1}$ | $8.2 \times 10^{13}$ | 62 | 62 |
| $MoTe_2/SnS_2$ | 220 nm | $5.8 \times 10^4$ mA $W^{-1}$ | $2.47 \times 10^{10}$ | $3.27 \times 10^4$ (%) | This work |

calculated the responsivity ($R$) and external quantum efficiency (EQE) at various wavelengths of incident light. The values of $R$ and EQE decreased as the wavelength of incident light was enhanced as shown in Fig. 7(b). Photoresponse of the device based on the $MoTe_2/SnS_2$ heterostructure was investigated as a function of time at different power intensities ($P$ = 11, 20, 35, 44 mW $cm^{-2}$) of the incident light at a wavelength $\lambda$ = 220 nm for $V_{ds}$ = 0.5 V shown in Fig. 7(c). We have seen that the photocurrent is enhanced as the power of radiant light is raised. Fig. 7(d) shows the IV curves under dark and incident light of different power intensity, and we can observe the change in $V_{oc}$ and $I_{sc}$. It is observed that as the incident light's intensity increases, the reverse current rises steadily under the light. This is due to greater electron–hole pairs being generated at the p-$MoTe_2$/n-$SnS_2$ junction because of the incoming light, increasing the reverse and forward currents. Furthermore, $V_{oc}$ is non-linear and the value of $I_{sc}$ is linearly reliant on the intensity of the laser light as shown in Fig. 7(e). The maximum values of $V_{oc}$ = 0.32 V and $I_{sc}$ = −0.40 nA were achieved at $P$ = 44 mW $cm^{-2}$. Furthermore, we added the Table 1 that summarizes the various characteristics of different photodetectors based on various 2D materials. The p-$MoTe_2$/n-$SnS_2$-based device exhibits remarkable optoelectronic and rectifying characteristics.

## Conclusion

Finally, on $Si/SiO_2$, we created a stable $MoTe_2/SnS_2$ vdW's heterostructure p–n diode. The device has a rectifying effect that is highly dependent on the back-gate voltage. One can create a vdW heterojunction p–n diode that performs the rectifying function in transparent and flexible electronics by using $MoTe_2$ and $SnS_2$ materials, respectively. Raman intensity mapping and XPS analysis are also employed to check the formation of the vdW heterostructure and quality of both materials $MoTe_2$ and $SnS_2$. A high rectification ratio of $2.79 \times 10^5$ and the lowest ideality factor ($\eta$) of about 1.25 were achieved. Prospective nano-electronic and optoelectronic technologies that rely on $MoTe_2$ and $SnS_2$ heterostructures would include a variety of FETs, photodetectors, and advanced photovoltaic cells. The maximum change in photocurrent ($I_{ph}$) is found to be about 90 nA. The device exhibited a high responsivity ($R$) of $5.8 \times 10^4$ mA $W^{-1}$, and the maximum EQE and detectivity are calculated to be about $3.27 \times 10^{4\%}$ and $2.47 \times 10^{10}$ Jones for the device, at $V_{ds}$ = 0.9 V for wavelength = 220 nm, respectively. Furthermore, the photoresponse of the device was also checked at different wavelengths of incident light, and with different power intensities of light. The p-$MoTe_2$/n-$SnS_2$-based device has excellent rectifying and optoelectronic properties. These heterojunctions should expand the possibilities for future nanoscale optoelectronic devices.

## Author contributions

H. N. and E. E. conceived and designed the experiments, MAK helped in device fabrication. J. J performed the AFM analysis. E. E. performed the electrical and photo (DUV) measurements of the devices. SKJ helps in XPS analysis and proofread the article. A. A Al-K performed the Raman mapping and obtained photoresponse data at different wavelengths. H. N. and E. E wrote the final manuscript. All the authors have approved the final version of the manuscript.

## Data availability statement

All data needed to evaluate the conclusions are present in this article and the ESI.† Additional data related to this article may be requested from the corresponding authors.

## Conflicts of interest

The authors declare that they have no competing interests.

## Acknowledgements

This research was supported by the National Research Foundation of Korea (NRF) grant funded by the Korea government (MSIT) (No. NRF-2020R1F1A1071556). The authors also thank the researchers supporting the project (RSP2023R266), and King Saud University, Riyadh, Saudi Arabia for their financial support.

## References

1 J. Zhou, *et al.*, A library of atomically thin metal chalcogenides, *Nature*, 2018, **556**(7701), 355–359.



 

2 F. Xia, H. Wang and Y. Jia, Rediscovering black phosphorus as an anisotropic layered material for optoelectronics and electronics, *Nat. Commun.*, 2014, **5**(1), 1–6.
3 J. Yao and G. Yang, 2D layered material alloys: Synthesis and application in electronic and optoelectronic devices, *Adv. Sci.*, 2022, **9**(1), 2103036.
4 P. Zomer, *et al.*, Long-distance spin transport in high-mobility graphene on hexagonal boron nitride, *Phys. Rev. B: Condens. Matter Mater. Phys.*, 2012, **86**(16), 161416.
5 E. Elahi, *et al.*, A review on two-dimensional (2D) magnetic materials and their potential applications in spintronics and spin-caloritronic, *Comput. Mater. Sci.*, 2022, **213**, 111670.
6 E. Elahi, *et al.*, A brief review on the spin valve magnetic tunnel junction composed of 2D materials, *J. Phys. D: Appl. Phys.*, 2022, **55**, 423001.
7 M. W. Iqbal, *et al.*, Enhancing the electronic properties of the graphene-based field-effect transistor via chemical doping of KBr, *J. Mater. Sci.: Mater. Electron.*, 2022, **33**(15), 12416–12425.
8 F. H. Koppens, D. E. Chang and F. J. García de Abajo, Graphene plasmonics: a platform for strong light–matter interactions, *Nano Lett.*, 2011, **11**(8), 3370–3377.
9 H. Tan, *et al.*, Ultrathin 2D photodetectors utilizing chemical vapor deposition grown WS2 with graphene electrodes, *ACS Nano*, 2016, **10**(8), 7866–7873.
10 F. Koppens, *et al.*, Photodetectors based on graphene, other two-dimensional materials and hybrid systems, *Nat. Nanotechnol.*, 2014, **9**(10), 780–793.
11 M. Iqbal, *et al.*, Chemical doping of transition metal dichalcogenides (TMDCs) based field effect transistors: A review, *Superlattices Microstruct.*, 2020, **137**, 106350.
12 M. W. Iqbal, *et al.*, A facile route to enhance the mobility of MoTe2 field effect transistor via chemical doping, *Superlattices Microstruct.*, 2020, **147**, 106698.
13 D. De Fazio, *et al.*, High responsivity, large-area graphene/MoS2 flexible photodetectors, *ACS Nano*, 2016, **10**(9), 8252–8262.
14 A. Pezeshki, *et al.*, Static and dynamic performance of complementary inverters based on nanosheet α-MoTe2 p-channel and MoS2 n-channel transistors, *ACS Nano*, 2016, **10**(1), 1118–1125.
15 Z. Sun, A. Martinez and F. Wang, Optical modulators with 2D layered materials, *Nat. Photonics*, 2016, **10**(4), 227–238.
16 J. A. Tatum and J. K. Guenter, *Consumer electronics with optical communication interface*. 2010, Google Patents.
17 M. Kang, *et al.*, Universal mechanism of band-gap engineering in transition-metal dichalcogenides, *Nano Lett.*, 2017, **17**(3), 1610–1615.
18 Q. H. Wang, *et al.*, Electronics and optoelectronics of two-dimensional transition metal dichalcogenides, *Nat. Nanotechnol.*, 2012, **7**(11), 699–712.
19 K. Novoselov, *et al.*, 2D materials and van der Waals heterostructures, *Science*, 2016, **353**(6298), aac9439.
20 P. K. Sahoo, *et al.*, One-pot growth of two-dimensional lateral heterostructures via sequential edge-epitaxy, *Nature*, 2018, **553**(7686), 63–67.
21 X. Zong, *et al.*, Black phosphorus-based van der Waals heterostructures for mid-infrared light-emission applications, *Light: Sci. Appl.*, 2020, **9**(1), 1–8.
22 H. Fang, *et al.*, Strong interlayer coupling in van der Waals heterostructures built from single-layer chalcogenides, *Proc. Natl. Acad. Sci. U. S. A.*, 2014, **111**(17), 6198–6202.
23 C.-H. Lee, *et al.*, Atomically thin p–n junctions with van der Waals heterointerfaces, *Nat. Nanotechnol.*, 2014, **9**(9), 676–681.
24 F. Wang, *et al.*, Tunable GaTe-MoS2 van der Waals p–n junctions with novel optoelectronic performance, *Nano Lett.*, 2015, **15**(11), 7558–7566.
25 B. Wang, *et al.*, Enhanced current rectification and self-powered photoresponse in multilayer p-MoTe 2/n-MoS 2 van der Waals heterojunctions, *Nanoscale*, 2017, **9**(30), 10733–10740.
26 A. Pezeshki, *et al.*, Electric and photovoltaic behavior of a few-layer α-MoTe2/MoS2 dichalcogenide heterojunction, *Adv. Mater.*, 2016, **28**(16), 3216–3222.
27 M. M. Furchi, *et al.*, Photovoltaic effect in an electrically tunable van der Waals heterojunction, *Nano Lett.*, 2014, **14**(8), 4785–4791.
28 S. H. A. Jaffery, *et al.*, Thickness-Dependent, Gate-Tunable Rectification and Highly Sensitive Photovoltaic Behavior of Heterostructured GeSe/WS2 p–n Diode, *Adv. Mater. Interfaces*, 2020, 7(23), 2000893.
29 C. Ruppert, B. Aslan and T. F. Heinz, Optical properties and band gap of single-and few-layer MoTe2 crystals, *Nano Lett.*, 2014, **14**(11), 6231–6236.
30 Y. F. Lin, *et al.*, Ambipolar MoTe2 transistors and their applications in logic circuits, *Adv. Mater.*, 2014, **26**(20), 3263–3269.
31 S. Hussain, *et al.*, Enhanced electrocatalytic properties in MoS2/MoTe2 hybrid heterostructures for dye-sensitized solar cells, *Appl. Surf. Sci.*, 2020, **504**, 144401.
32 Z. Feng, *et al.*, Highly sensitive MoTe2 chemical sensor with fast recovery rate through gate biasing, *2D Mater.*, 2017, **4**(2), 025018.
33 A. Joseph, *et al.*, Structural, optical and magnetic properties of SnS2 nanoparticles and photo response characteristics of p-Si/n-SnS2 heterojunction diode, *Appl. Surf. Sci.*, 2020, **528**, 146977.
34 L. A. Burton, *et al.*, Synthesis, characterization, and electronic structure of single-crystal SnS, Sn2S3, and SnS2, *Chem. Mater.*, 2013, **25**(24), 4908–4916.
35 G. Su, *et al.*, Chemical vapor deposition of thin crystals of layered semiconductor SnS2 for fast photodetection application, *Nano Lett.*, 2015, **15**(1), 506–513.
36 K. Chen, *et al.*, Accelerated carrier recombination by grain boundary/edge defects in MBE grown transition metal dichalcogenides, *APL Mater.*, 2018, **6**(5), 056103.
37 T. J. Whittles, *et al.*, Band alignments, valence bands, and core levels in the tin sulfides SnS, SnS2, and Sn2S3: experiment and theory, *Chem. Mater.*, 2016, **28**(11), 3718–3726.
38 A. Kumar, S. Vinayak and R. Singh, Micro-structural and temperature dependent electrical characterization of Ni/GaN Schottky barrier diodes, *Curr. Appl. Phys.*, 2013, **13**(6), 1137–1142.

39 T. Hong, *et al.*, Anisotropic photocurrent response at black phosphorus–MoS 2 p–n heterojunctions, *Nanoscale*, 2015, **7**(44), 18537–18541.
40 P. Chen, *et al.*, Gate tunable MoS2–black phosphorus heterojunction devices, *2D Mater.*, 2015, **2**(3), 034009.
41 H. Fang, *et al.*, Visible light-assisted high-performance mid-infrared photodetectors based on single InAs nanowire, *Nano Lett.*, 2016, **16**(10), 6416–6424.
42 P. Wang, *et al.*, Arrayed van der Waals broadband detectors for dual-band detection, *Adv. Mater.*, 2017, **29**(16), 1604439.
43 A. Pospischil, M. M. Furchi and T. Mueller, Solar-energy conversion and light emission in an atomic monolayer p–n diode, *Nat. Nanotechnol.*, 2014, **9**(4), 257–261.
44 Y. Jin, *et al.*, A van der Waals homojunction: ideal p–n diode behavior in MoSe2, *Adv. Mater.*, 2015, **27**(37), 5534–5540.
45 G. Dastgeer, *et al.*, Temperature-dependent and gate-tunable rectification in a black phosphorus/WS2 van der Waals heterojunction diode, *ACS Appl. Mater. Interfaces*, 2018, **10**(15), 13150–13157.
46 K. Murali, *et al.*, Gate-tunable WSe2/SnSe2 backward diode with ultrahigh-reverse rectification ratio, *ACS Appl. Mater. Interfaces*, 2018, **10**(6), 5657–5664.
47 H. Luo, *et al.*, High-responsivity photovoltaic photodetectors based on MoTe2/MoSe2 van der Waals heterojunctions, *Crystals*, 2019, **9**(6), 315.
48 N. Oliva, *et al.*, van der Waals MoS2/VO2 heterostructure junction with tunable rectifier behavior and efficient photoresponse, *Sci. Rep.*, 2017, **7**(1), 14250.
49 M. Hussain, *et al.*, NIR self-powered photodetection and gate tunable rectification behavior in 2D GeSe/MoSe2 heterojunction diode, *Sci. Rep.*, 2021, **11**(1), 3688.
50 Y. Deng, *et al.*, Black phosphorus–monolayer MoS2 van der Waals heterojunction p–n diode, *ACS Nano*, 2014, **8**(8), 8292–8299.
51 K. J. Baeg, *et al.*, Organic light detectors: photodiodes and phototransistors, *Adv. Mater.*, 2013, **25**(31), 4267–4295.
52 M. Buscema, *et al.*, Fast and broadband photoresponse of few-layer black phosphorus field-effect transistors, *Nano Lett.*, 2014, **14**(6), 3347–3352.
53 C. Lan, *et al.*, Zener tunneling and photoresponse of a WS2/Si van der Waals heterojunction, *ACS Appl. Mater. Interfaces*, 2016, **8**(28), 18375–18382.
54 M. F. Khan, *et al.*, Bipolar Photoresponse of a Graphene Field-Effect Transistor Induced by Photochemical Reactions, *ACS Appl. Electron. Mater.*, 2023, **5**(9), 5111–5119.
55 K. Gong, *et al.*, High detectivity and fast response avalanche photodetector based on GaSe/$PtSe_2$ p–n junction, *Mater. Des.*, 2023, **228**, 111848.
56 A. Varghese, *et al.*, Near-direct bandgap WSe2/ReS2 type-II pn heterojunction for enhanced ultrafast photodetection and high-performance photovoltaics, *Nano Lett.*, 2020, **20**(3), 1707–1717.
57 L. Ye, *et al.*, Near-infrared photodetector based on MoS2/black phosphorus heterojunction, *ACS Photonics*, 2016, **3**(4), 692–699.
58 L. H. Zeng, *et al.*, Fast, self-driven, air-Stable, and broadband photodetector based on vertically aligned PtSe2/GaAs heterojunction, *Adv. Funct. Mater.*, 2018, **28**(16), 1705970.
59 J. Zhang, *et al.*, Modulating the Function of GeAs/ReS2 van der Waals Heterojunction with its Potential Application for Short-Wave Infrared and Polarization-Sensitive Photodetection, *Small*, 2023, 2303335.
60 Z. He, *et al.*, GaSe/MoS2 Heterostructure with Ohmic-Contact Electrodes for Fast, Broadband Photoresponse, and Self-Driven Photodetectors, *Adv. Mater. Interfaces*, 2020, **7**(9), 1901848.
61 Y. Ren, *et al.*, *Interface Engineering Sns2/Mxene Nb2c Self-Powered Photodetectors with High Responsivity and Detectivity*. Available at SSRN 4414683.
62 P. Perumal, *et al.*, Staggered band offset induced high performance opto-electronic devices: Atomically thin vertically stacked GaSe-SnS2 van der Waals pn heterostructures, *Appl. Surf. Sci.*, 2021, **535**, 147480.

 